

In situ observation of compression damage in a 3D needled-punched carbon fiber-silicon carbide ceramic matrix composite¹

Short title: μ XCT of Compressive Damage in a needled-punched C-SiC composite

Fan Wan^{1, 2}, Rongjun Liu¹, Yanfei Wang¹, Yingbin Cao¹, Changrui Zhang¹ and Thomas James Marrow^{*2}

1. Science and Technology on Advanced Ceramic Fibers and Composites Laboratory,
National University of Defense Technology, Changsha, 410073, China
2. Department of Materials,
University of Oxford, Oxford, OX1 3PH, UK

*Corresponding Author:

Thomas James Marrow, james.marrow@materials.ox.ac.uk

tel: +44 7540 722660

¹ This is the author's copy of a manuscript that was accepted for publication in 'Composite Structures',
<https://doi.org/10.1016/j.compstruct.2018.11.041>

Abstract

Damage development has been observed in situ within a 3-dimensional needle-punched carbon fiber reinforced carbon and silicon carbide (C/C-SiC) ceramic composite, as compressive loads were applied longitudinally, transversely and obliquely to its anisotropic structure. Laboratory X-ray computed tomographs were analyzed using digital volume correlation to measure the local strains. Cracks exist within the microstructure before the application of load, due to thermal strains, and their propagation is affected by the heterogeneous microstructure and the direction of loading. The punched carbon fiber needles are observed to restrict the propagation of damage.

Key Words

C/C-SiC; Ceramic matrix composite; Compressive damage; 3D needled-punched; X-ray Computed Tomography; Digital Volume Correlation

1 Introduction

3D needle-punched carbon fiber felts or non-woven cloths are widely used as the reinforcement [1–5] in C/C and C/C-SiC composites, because of their relatively low economic cost compared to 3D braided felts and good structural mechanical properties compared to short-cut fiber felts. Due to the complex structures of needle-punched ceramic composites, previous research has sought to understand the relationship between structure and mechanical properties. For instance, Zhang et al. [6] investigated the relations between the compressive properties of 3D needle-punched C/C composites and the matrix structure, and found that samples with dual matrix (CVI and PIP carbon) showed higher strength and catastrophic failure behavior while samples with single CVI matrix had lower strength and exhibited a more graceful quasi-brittle fracture behavior. Li et al. [7] observed the effect of test temperature on the compression properties and failure mechanism of 3D needle-punched C/C composite, finding a transition from brittle shear failure to more ductile behaviour above 600°C due to a decrease in the interfacial adhesion between fibers and matrix. Peng et al. [8] studied the monotonic tensile response, damage development and acoustic emission activity of 3D needle-punched C/SiC composite, observing a beneficial effect of interfacial PyC and pores in the matrix on microcracking damage that initiated at low fractions of the strength. Xie et al. [9] conducted room temperature and high temperature (800°C, 1200°C, 1500°C and 1800°C) tensile tests of a 3D needled C/C-SiC composite and established a nonlinear constitutive model to describe the stress-strain relationships. Chen et al. [10] conducted in-plane tensile experiments of 3D needle-punched C/C-SiC composites from room temperature to 2000°C to study the microscopic failure mechanisms, finding that relaxation of thermal residual stresses tended to counteract the effects of decreasing the interfacial strength, but increasing SiC crystallization degraded the strength of the matrix at higher temperature. To date, no studies have been published that investigate the inter-relationship between the mechanical response and the microstructure components (i.e. fiber cloth, short-cut web and needle). The available analyses of the

fracture mechanism and damage patterns [6,7,9,11] were all post-mortem investigations, and as such provided limited information on the sequence of damage development and the microstructure components from which it initiated.

X-ray computed tomography (XCT) is a nondestructive imaging technique that can provide in situ observations and both qualitative and quantitative information of structure within materials [12]. Studies during mechanical testing, some at elevated temperatures, have provided insights into damage development in a wide range of materials, including metals [13], metal matrix composites [14,15], polygranular graphite [16], gypsum [17] and ceramic matrix composites [18,19]. Digital Volume Correlation (DVC) measures the relative deformations between successive tomographs, using contrast from the heterogeneities in the microstructure (e.g. porosity and phases), and has been applied to investigate mechanical damage processes in materials as diverse as compacted particulates [20], wood [21,22], metallic alloys [23–25], polygranular nuclear graphite [26,27], concrete [28] and ceramic matrix composites [29,30].

Recently, some of the authors examined damage development in a 3D braided carbon-fiber/SiC composite, using DVC of XCT images to observe the propagation of internal cracks under compressive loading [31]. The propagation of cracks that had initiated during material fabrication, and their interaction with the braided structures was sensitive to the stress direction in the microstructure. Compression damage in woven C/SiC composites has been observed to be sensitive to the local structures [32], and needle-punched composites also have significant structure complexity, with parameters of needle-punch density and punch length that need to be optimised [33]. Insights gained from in situ observations of the damage process can be useful in materials design and also in the verification of materials modelling. In this paper, a 3D needle-punched C/C–SiC composite has been studied, in situ, under compressive loading to observe how mechanical damage evolves from

structure's components with increasing load. The objective was to verify the role of the needle-punched fibers in the improvement of material integrity.

2 Experimental

2.1 Material

Chemical vapor deposition (CVD) was used to generate the C/C porous material (density 1.28 g/cm³, T-300 carbon fiber) based on 3D needle-punched fabric preform [2], which was provided by the Composites Institute of Tianjing Technology University (China). In this process, non-woven cloths of aligned fibers and short-cut webs of non-aligned fibers are stacked. The needle punching of carbon fiber stitches is used to link adjacent layers to obtain the fabric preform. The C/C-SiC composite was manufactured by Gaseous Silicon Infiltration (GSI) in the Laboratory of Science and Technology on Advanced Ceramic Fibers and Composites at the National University of Defense Technology (China). In this process, the C/C perform was reacted with gaseous silicon at 1700°C to achieve a final density of 2.0 g/cm³. Cutting of the test specimens was done at the Department of Materials, University of Oxford, with a water-cooled diamond saw (0.6 mm blade width).

2.2 In Situ Tomography

Compression tests, in three different orientations with respect to the microstructure (longitudinal, transverse and oblique), were done between flat stainless steel anvils using a Deben CT5000 loading rig (5 kN load capacity)². This was mounted within an Xradia Versa 510 X-ray microscope, operated

² See <https://deben.co.uk/tensile-testing/mxct/tensile-stages-for-x-ray-ct-tomography/> for details of this standard μ XCT loading stage set-up on an Xradia Versa microscope.

at 80 keV energy and 7 W power. Each specimen was observed at a pre-load of 20 N, and then with progressively higher loads applied using displacement control of the loading rig. The specimen dimensions ($x \times z \times y$) were nominally 5 mm \times 4 mm \times 10 mm. The actual dimensions were 4.7 mm \times 3.8 mm \times 9.4 mm, 4.3 mm \times 3.8 mm \times 9.9 mm and 4.6 mm \times 3.8 mm \times 9.7 mm for the longitudinal, transverse and oblique specimens respectively.

Each tomograph was reconstructed from 1601 projections recorded over a 360° rotation, with 2x binning of the 2048 \times 2048 pixel camera. Imaging was done at two different voxel sizes, 11.5 μ m and 5 μ m, to observe both the bulk of the specimen and a smaller region of interest. The exposure times for the 11.5 μ m and 5 μ m voxel tomographs were 4 s and 10 s per projection, respectively, with each scan requiring either 2 hours and 40 minutes or 6 hours. The observed volumes at 11.5 μ m voxel resolution has dimensions ($x \times z \times y$) of 4.5 mm \times 3.6 mm \times 7.9 mm (longitudinal), 4.1 mm \times 3.6 mm \times 8.1 mm (transverse) and 4.3 mm \times 3.6 mm \times 8.5 mm (oblique); at 5 μ m voxel resolution the vertical dimension in the y direction was restricted to 5 mm. The tomographs were reconstructed using the instrument software, and were visualized using the software Avizo 9.3.0.

3 Results and Discussion

3.1 Microstructure Characterization

An example tomograph (5 μ m voxel) of the 3D needle-punched microstructure is shown in Figure 1a, with the non-woven fiber cloth directions (0° and 90°, according to the fiber direction in the cloth) and the orthogonal needle direction (N) defined. The layered structure of non-woven cloths is clearly seen, with the fiber bundles in the cloths separated by the introduction of the needle-punch. A schematic of the microstructure is shown in Figure 1b. Parallel slices (A-C) of the tomograph, perpendicular to the needle direction (Figure 1c-e) show the characteristics of the 0° cloth, the 90° cloth and short-cut web that is between them. Some initial cracks can be observed within the fiber cloths, between the fibers.

Porosity are observed, especially in the short-cut web area and needled area, with some pores having a linear dimension up to 1 mm. The main fiber bundles of the 0° and 90° cloths and the stitched needles were segmented using greyscale thresholding and their arrangement (Figure 2) shows how the cloth layers are affected by the punched needles.

Segmentation by greyscale thresholding was also used to measure the pore volume (Figure 3a). Similar data were obtained at the two image resolutions, with smaller pores better resolved at high resolution. A good agreement is obtained with the ~16% porosity measured by gravimetric analysis [2], and also the fiber and matrix volume fractions (Table 1). The spatial variation of pores, fiber and matrix was measured along the orthogonal directions in a series of 2D slices of the tomograph from Figure 1a. The layered structure causes periodic correlated fluctuations of the constituents (Figure 3b) with a wavelength of ~1.1 mm, with the proportions of fibers, matrix and pores along the orthogonal 90° (Figure 3c) and 0° (Figure 3d) cloth directions being approximately constant.

3.2 Damage Development

Tomographs of the specimens, recorded prior to testing, are shown in Figure 4 with the y-axis loading direction indicated. The cloths directions of 0° and 90° are defined, using the fiber axes, to simplify the discussion when considering the longitudinal and oblique loading tests. In principal, they are exactly equivalent for the transverse loading case. The load-crosshead displacement curves (Figure 5) are marked with the loads at which tomographs were recorded; loading was paused to record each tomograph, during which a small amount (~5%) of relaxation occurred. The final fracture of the longitudinal and oblique specimens was catastrophic, with more graceful failure of the transverse specimen. The peak loads in the longitudinal, transverse and oblique tests were 4020 N, 2950 N and 2050 N respectively, corresponding to compressive stresses of 225 MPa, 180 MPa and 117 MPa. Tomographs recorded after failure, at 11.5 µm voxel resolution, are shown in Figure 6, with the main cracks identified by image segmentation. The longitudinal specimen has mostly vertical major cracks,

parallel to the cloth layers, connected by a shear failure. The transverse sample has developed quite complex damage throughout its volume, also generally parallel to the cloth layers. The oblique specimen has sheared along the plane of a 0° cloth layer.

Internal cracks within the carbon fiber cloths can be observed in the tomographs recorded at 20 N (Figure 7). These cracks are between the fibers, and on loading tended to close when the fibers are perpendicular to the applied compressive load. This is illustrated by several examples, highlighted by dashed rectangular boxes, for longitudinal compression (Figure 7a and Figure 7b) and transverse compression (Figure 7c). In regions where the fibers of the cloth are parallel to the load, splitting and interface failure (Figure 7a) and kinking (Figure 7b) occurred; these are indicated by dashed circles in the figures. Cracks that are parallel to the applied load are observed to have developed in the matrix of both the needle punched regions (Figure 7b) and short cut web (Figure 7c).

Six characteristic types of crack-like damage can be identified: interfacial debonding between the matrix and the 90° and 0° cloths, internal fractures within the 90° and 0° cloths and internal fractures of the matrix in the short-cut web or at the stitched needles. Their development with increasing load is visualized in Figure 8, using color to label the different types. For longitudinal loading (Figure 8a), cracking developed mostly parallel to the load, with internal and interfacial cracks of the 90° cloth dominating; no needle cracks and short-cut web cracks can be observed until 3500 N, which was close to the final failure load. Prior to the catastrophic failure, less damage was observed to develop under transverse loading; it was concentrated towards one location (Figure 8b) and comprised internal cracking and debonding of both 0° and 90° cloths, as well as cracking in the short cut web and within the needle stitch cracks. For oblique loading, the dominant cracks initially tended to develop within the 0° cloth, in which the fibers were aligned perpendicular to the load. These cracks propagated mostly as interfacial debonding (Figure 8c).

The thermal expansion of Silicon carbide [34] is intermediate between the longitudinal and transverse thermal expansion of carbon fiber [35], which has a lower thermal expansion longitudinally compared to its transverse direction. The composite is fabricated by GSI at elevated temperature. Consequently, tensile strains may be expected to develop in the silicon carbide matrix with compression along the carbon fibers, but the largest tensile thermal strains will act orthogonally to the non-woven cloths due to the high transverse thermal expansion coefficient of the fibers. The interfaces between the fibers within the cloths cannot sustain significant tensile strain, thus internal cracking occurs readily, as observed (Figure 7). The tensile thermal strains will also aid interfacial debonding of the non-woven cloths, and may encourage fracture of the SiC matrix.

3.3 Digital Volume Correlation Analysis

The digital volume correlation (DVC) analysis of the tomographs used the LaVision Davis software (version 8.4.0), with the initial tomograph at 20 N as the reference. Image correlation tracks the relative movements and deformations of subsets of the images, and to achieve high spatial resolution, a small final subset size ($24 \times 24 \times 24$ voxels, 75% overlap, 2 passes) was used after preliminary larger subset sizes $128 \times 128 \times 128$ (75% overlap, 2 passes) and $64 \times 64 \times 64$ (75% overlap, 2 passes) that used FFT (fast Fourier transform) correlation. The center of the volume was made the origin for the relative displacements by applying a uniform rigid body displacement with no rotation. The data were cropped to approximately $4.1 \text{ mm} \times 3.4 \text{ mm} \times 7.8 \text{ mm}$, $3.8 \text{ mm} \times 3.4 \text{ mm} \times 7.8 \text{ mm}$ and $4.0 \text{ mm} \times 3.4 \text{ mm} \times 8.3 \text{ mm}$ for the longitudinal (Figure 9a), transverse (Figure 9b), and oblique (Figure 9c) specimens respectively by removing the potentially inaccurate displacement vectors calculated from subsets that approached the edges of tomographed volume. Example displacement fields measured at 750 N, before significant damage occurred, are presented in Figure 9 and show the quite complex deformations; for instance, shearing parallel to the non-woven cloths in both the transverse (Figure 9b) and oblique (Figure 9c) specimens.

To illustrate how the deformation has been accommodated by the microstructure, gradients of the three-dimensional displacement field, at the highest observed loading (3500 N, 2500 N and 1500 N for longitudinal, transverse and oblique samples respectively), are presented in Figure 10 as normal strains (ϵ_{xx} , ϵ_{yy}) that are parallel to the x and y axes, shear strain (ϵ_{xy}) in the same plane and the maximum three-dimensional principal strain. The compression of the longitudinal specimen, in which the cloths were vertically aligned, was applied parallel to the fibers of the 90° non-woven cloth and perpendicular to the fibers of the 0° cloth; there are local tensile strains (ϵ_{xx}) that develop perpendicular to the 90° cloths (Figure 10a i), whilst local compressive strains (ϵ_{yy}) parallel to the applied load occur within the 0° non-woven cloth (Figure 10a ii). This is consistent with the observed opening of internal cracks between the fibers in the 90° cloths (Figure 7a) and short cut web matrix (Figure 7b) and the closure of pores and internal cracks between the fibers of the 0° cloth (Figure 7a and b). The transverse specimen shows concentrations of compressive strain (ϵ_{yy}) in the 0° and 90° cloths, which are both horizontal and perpendicular to the applied load (Figure 10b ii). Tensile strains (ϵ_{xx}) perpendicular to the applied load also develop (Figure 10b i). These strains are in agreement with the observation of compressive closure of pre-existing defects in the cloths (Figure 7c) and the orthogonal opening of cracks between fibers and initiation of cracks within the short cut web (Figure 7c). For the oblique loaded specimen, compressive (ϵ_{yy}), tensile (ϵ_{xx}) and shear strains (ϵ_{xy}) are all concentrated within the 0° cloth layers (Figure 10c), and this is consistent with shear propagation of damage between the fibers that are aligned perpendicular to the load. The detection of cracks by tomography alone is less sensitive than the measurement of strain by digital volume correlation of tomographs; cracks can only be observed by tomography when the crack opening approaches the voxel size, whereas digital volume correlation can detect sub-voxel displacements and the cumulative effects of microcracking, such as may occur between fibers.

3.4 *Effects of Needle-Stitching on Damage Propagation*

The maximum 3D principal strain identifies the location of the characteristic damage mechanisms, which are: internal fracture and debonding of the vertical 90° cloth (Figure 10a iv and Figure 8a) under longitudinal loading; internal fracture of both cloths and matrix under transverse loading (Figure 10b iv and Figure 8b); and internal fracture and debonding of the 0° cloth under oblique loading (Figure 10c iv and Figure 8c). Consequently, the maximum principal strain can be used to visualize the damage. Figure 11 illustrates the relationship between the needle stitching and the final damage distribution in the longitudinal compression test; the figure shows the positions of the cracks relative to the needles. The images (1) to (4) show slices through the three-dimensional data. This shows the effect of the needles on damage propagation. The maximum principal strain (Figure 10a) reveals that damage occurs in planar features that are coincident with the 90° cloths, at which internal splitting and interfacial debonding were observed by tomography (Figure 6a). The propagation of damage within the cloths is clearly restricted by the needles (Figure 11). This restriction in the propagation of damage is considered to be responsible for the higher strength and high failure strain in the longitudinal test (Figure 5).

The observations of the intrinsic defects in the microstructure, their propagation under load and the effects of the needles on damage are used to propose sequences for the development of the main failures under different loading states, which are shown schematically in Figure 12. Under longitudinal loading (Figure 12a), (i) interfacial cracks predominantly propagate along the 90° cloths due to the splitting effect of the Poisson strains, but (ii) are limited by the pinning effect of the needles; (iii) final shear failure occurs when the extensive damage coalesces. For transverse loading (Figure 12b), the effect of the needles is less significant as (i) the propagation of tensile damage under action of the Poisson strains is limited by the fiber cloths; so (ii) interfacial fractures are driven by stress concentrations from the distorted cloths and heterogeneities of the elastic moduli; until (iii) final shear

by coalescence occurs. Under the action of the oblique load (Figure 12c), (i) the fractures that propagate most readily are those between the fibers within the 0° cloth, which offer a weaker resistance to shear than the 90° cloth in which the long fibers are parallel to the shear loading; (ii) these internal fractures then propagate along the cloth interface to accommodate the shear loading. The needles would be expected to retard damage development, but this was not observed as the localized damage in the small specimen leads to instability and then (iii) localized shear failure from a dominant crack.

4 Conclusion

Compression failure of 3D needle-punched C/C-SiC composites is affected by microstructure, principally due to the intrinsic defects that exist after processing. These defects are deduced to be caused by differences in thermal expansion between the constituents. In longitudinal compression, high strength arises from the stabilizing effect of the stitches introduced by needle-punching, which are quite effective in resisting the propagation of interfacial cracks between the non-woven cloths and the matrix.

5 Acknowledgements

We acknowledge EPSRC Grant EP/M02833X/1 “University of Oxford: experimental equipment upgrade”, which supported the Xradia Versa 510 microscope and facilities for data analysis and visualization. The research is part of the Project 2018JJ1029 supported by Hunan Provincial Natural Science Foundation of China. The work was conducted at Oxford University, with China Scholarship Council support for Wan Fan as a recognized student.

6 References

- [1] Xiao P, Li Z, Xiong X. Microstructure and tribological properties of 3D needle-punched C/C–SiC brake composites. *Solid State Sciences* 2010;12:617–23. doi:<https://doi.org/10.1016/j.solidstatesciences.2010.01.014>.
- [2] Nie J, Xu Y, Zhang L, Fan S, Xu F, Cheng L, et al. Microstructure, Thermophysical, and Ablative Performances of a 3D Needled C/C–SiC Composite. *International Journal of Applied Ceramic Technology* n.d.;7:197–206. doi:10.1111/j.1744-7402.2008.02341.x.
- [3] Wang H, Zhu D, Wan F, Zhou W, Luo F. Influence of the C/C preform density on tribological characteristics of C/C–SiC composites under different conditions. *Ceramics International* 2014;40:16641–6. doi:10.1016/j.ceramint.2014.08.025.
- [4] Li Z, Xiao P, Zhang B gu, Li Y, Lu Y hai. Preparation and tribological properties of C/C–SiC brake composites modified by in situ grown carbon nanofibers. *Ceramics International* 2015;41:11733–40. doi:10.1016/j.ceramint.2015.05.139.
- [5] Tong Y, Bai S, Qin QH, Zhang H, Ye Y. Effect of infiltration time on the microstructure and mechanical properties of C/C–SiC composite prepared by Si–Zr10 alloyed melt infiltration. *Ceramics International* 2015;41:4014–20. doi:<https://doi.org/10.1016/j.ceramint.2014.11.088>.
- [6] Zhang J, Luo R, Xiang Q, Yang C. Compressive fracture behavior of 3D needle-punched carbon/carbon composites. *Materials Science and Engineering: A* 2011;528:5002–6. doi:<https://doi.org/10.1016/j.msea.2011.03.055>.
- [7] Li D, Luo G, Yao Q, Jiang N, Jiang L. High temperature compression properties and failure mechanism of 3D needle-punched carbon/carbon composites. *Materials Science and Engineering: A* 2015;621:105–10. doi:<https://doi.org/10.1016/j.msea.2014.10.060>.
- [8] Fang P, Cheng L, Zhang L, Nie J. Monotonic tensile behavior analysis of three-dimensional needle-punched woven C/SiC composites by acoustic emission. *Journal of University of Science and Technology Beijing, Mineral, Metallurgy, Material* 2008;15:302–6. doi:[https://doi.org/10.1016/S1005-8850\(08\)60057-2](https://doi.org/10.1016/S1005-8850(08)60057-2).
- [9] Xie J, Fang G, Chen Z, Liang J. High-temperature constitutive model for three-dimensional needled C/C–SiC composite under tensile loading. *Journal of Composite Materials* 2016;51:2619–29. doi:10.1177/0021998316674350.
- [10] Chen Z, Fang G, Xie J, Liang J. Experimental study of high-temperature tensile mechanical properties of 3D needled C/C–SiC composites. *Materials Science and Engineering: A* 2016;654:271–7. doi:<https://doi.org/10.1016/j.msea.2015.12.010>.
- [11] Chen Z, Fang G, Xie J, Liang J. Mechanism-based strength criterion for 3D needled C/C–SiC composites under in-plane biaxial compression. *Mechanics of Advanced Materials and Structures* 2018;6494:1–8. doi:10.1080/15376494.2018.1452316.
- [12] Duchene P, Chaki S, Ayadi A, Krawczak P. A review of non-destructive techniques used for

-
- mechanical damage assessment in polymer composites. *Journal of Materials Science* 2018;53:7915–38. doi:10.1007/s10853-018-2045-6.
- [13] King A, Ludwig W, Herbig M, Buffière J-Y, Khan AA, Stevens N, et al. Three-dimensional in situ observations of short fatigue crack growth in magnesium. *Acta Materialia* 2011;59:6761–71. doi:<https://doi.org/10.1016/j.actamat.2011.07.034>.
- [14] Withers PJ, Bennett J, Hung Y-C, Preuss M. Crack opening displacements during fatigue crack growth in Ti–SiC fibre metal matrix composites by X-ray tomography. *Materials Science and Technology* 2006;22:1052–8. doi:10.1179/174328406X114108.
- [15] Chapman NC, Silva J, Williams JJ, Chawla N, Xiao X. Characterisation of thermal cycling induced cavitation in particle reinforced metal matrix composites by three-dimensional (3D) X-ray synchrotron tomography. *Materials Science and Technology* 2015;31:573–8. doi:10.1179/1743284714Y.0000000582.
- [16] Vertyagina Y, Marrow TJ. Multifractal-based assessment of Gilsocarbon graphite microstructures. *Carbon* 2016;109:711–8. doi:<https://doi.org/10.1016/j.carbon.2016.08.049>.
- [17] Kong L, Ostadhassan M, Li C, Tamimi N. Pore characterization of 3D-printed gypsum rocks: a comprehensive approach. *Journal of Materials Science* 2018;53:5063–78. doi:10.1007/s10853-017-1953-1.
- [18] Zou C, Marrow TJ, Reinhard C, Li B, Zhang C, et al. Porosity characterization of fiber-reinforced ceramic matrix composite using synchrotron X-ray computed tomography. *Journal of Instrumentation* 2016;11:C03052.
- [19] Bale HA, Haboub A, Macdowell AA, Nasiatka JR, Parkinson DY, Cox BN, et al. Real-time quantitative imaging of failure events in materials under load at temperatures above 1,600°C. *Nature Materials* 2013;12:40–6. doi:10.1038/nmat3497.
- [20] Forsberg F and Siviour C. 3D deformation and strain analysis in compacted sugar using x-ray microtomography and digital volume correlation. *Measurement Science and Technology* 2009;20:95703.
- [21] Forsberg F, Mooser R, Arnold M, Hack E, Wyss P. 3D micro-scale deformations of wood in bending: Synchrotron radiation μ CT data analyzed with digital volume correlation. *Journal of Structural Biology* 2008;164:255–62. doi:<https://doi.org/10.1016/j.jsb.2008.08.004>.
- [22] Forsberg F, Sjö Dahl M, Mooser R, Hack E, Wyss P.. Full Three-Dimensional Strain Measurements on Wood Exposed to Three-Point Bending: Analysis by Use of Digital Volume Correlation Applied to Synchrotron Radiation Micro-Computed Tomography Image Data. *Strain* 2010;46:47–60. doi:10.1111/j.1475-1305.2009.00687.x.
- [23] Cai B, Lee PD, Karagadde S, Marrow TJ, Connolley T. Time-resolved synchrotron tomographic quantification of deformation during indentation of an equiaxed semi-solid granular alloy. *Acta Materialia* 2016;105:338–46. doi:<https://doi.org/10.1016/j.actamat.2015.11.028>.
- [24] Mostafavi M, Bradley R, Armstrong DEJ, Marrow TJ. Quantifying yield behaviour in metals by X-ray nanotomography. *Scientific Reports* 2016;6:34346.

-
- [25] Mostafavi M, Collins DM, Cai B, Bradley R, Atwood RC, Reinhard C, et al. Yield behavior beneath hardness indentations in ductile metals, measured by three-dimensional computed X-ray tomography and digital volume correlation. *Acta Materialia* 2015;82:468–82. doi:<https://doi.org/10.1016/j.actamat.2014.08.046>.
- [26] Marrow TJ, Liu D, Barhli SM, Saucedo Mora L, Vertyagina Y, Collins DM, et al. In situ measurement of the strains within a mechanically loaded polygranular graphite. *Carbon* 2016;96:285–302. doi:<https://doi.org/10.1016/j.carbon.2015.09.058>.
- [27] Barhli SM, Saucedo-Mora L, Jordan MSL, Cinar AF, Reinhard C, Mostafavi M, et al. Synchrotron X-ray characterization of crack strain fields in polygranular graphite. *Carbon* 2017;124:357–71. doi:<https://doi.org/10.1016/j.carbon.2017.08.075>.
- [28] Yang Z, Ren W, Sharma R, McDonald S, Mostafavi M, Vertyagina Y, et al. In-situ X-ray computed tomography characterisation of 3D fracture evolution and image-based numerical homogenisation of concrete. *Cement and Concrete Composites* 2017;75:74–83. doi:<https://doi.org/10.1016/j.cemconcomp.2016.10.001>.
- [29] Saucedo - Mora L, Zou C, Lowe T, Marrow TJ. Three-dimensional measurement and cohesive element modelling of deformation and damage in a 2.5-dimensional woven ceramic matrix composite. *Fatigue & Fracture of Engineering Materials & Structures* 2016;40:683–95. doi:10.1111/ffe.12537.
- [30] Saucedo-Mora L, Lowe T, Zhao S, Lee PD, Mummery PM, Marrow TJ. In situ observation of mechanical damage within a SiC-SiC ceramic matrix composite. *Journal of Nuclear Materials* 2016;481:13–23. doi:<https://doi.org/10.1016/j.jnucmat.2016.09.007>.
- [31] Wan F, Zhao S, Liu R, Zhang C and Marrow TJ. In-situ observation of compression damage in a 3D braided carbon fiber reinforced carbon and silicon carbide (C/C-SiC) ceramic composite. *Microscopy and Microanalysis* 2018.
- [32] Wang M, Laird C. Damage and fracture of a cross woven C/SiC composite subject to compression loading. *Journal of Materials Science* 1996;31:2065–9. doi:10.1007/BF00356628.
- [33] Xie J, Fang G, Chen Z, Liang J. Numerical and experimental studies on scattered mechanical properties for 3D needled C/C-SiC composites. *Composite Structures* 2018;192:545–54. doi:10.1016/j.compstruct.2018.03.056.
- [34] Li Z, Bradt RC. Thermal expansion of the cubic (3C) polytype of SiC. *Journal of Materials Science* 1986;21:4366–8. doi:10.1007/BF01106557.
- [35] Pradere C, Sauder C. Transverse and longitudinal coefficient of thermal expansion of carbon fibers at high temperatures (300-2500 K). *Carbon* 2008;46:1874–84. doi:10.1016/j.carbon.2008.07.035.

7 Figure Captions

Figure 1: Microstructure of the C/C-SiC composite: a) tomograph (voxel size 5 μm); b) schematic arrangement of microstructure; c) to e) slices of the tomograph at layers A to C.

Figure 2: Segmented image of microstructure (5 μm voxel tomograph): a) complete structure, separated in b) 90° non-woven cloth; c) 0° non-woven cloth and d) stitched needles.

Figure 3: Measurement of the observed porosity: a) contribution by size to the total porosity observed at 5 μm and 11.5 μm voxel resolution; average porosity per slice as a function of distance parallel to the fiber directions in the b) needle; c) 90° and d) 0° non-woven cloths.

Figure 4: Tomography visualisations (11.5 μm voxel) of the specimens before testing for a) longitudinal; b) transverse and c) oblique loading orientations.

Figure 5: Load versus crosshead displacement curves for the tested specimens. The loads are indicated at which 5 μm and 11.5 μm voxel resolution tomographs were recorded.

Figure 6: Tomography visualisations (11.5 μm voxel) of the specimens after testing for a) longitudinal; b) transverse and c) oblique loading orientations. The microstructure and major cracks are shown in i) and the segmented cracks are shown from different viewing positions in ii) and iii).

Figure 7: The development of damage with load, viewed in vertical orthoslices of 5 μm voxel tomographs: a) longitudinal specimen at i) 20 N and ii) 3500 N load (inset zoomed images show the dotted boxes, and dotted circles indicate damage within and at the interface of the non-woven cloth; b) longitudinal specimen at i) 20 N and ii) 3500 N load (dotted circles indicate fiber kinking at a pore within the non-woven cloth, and matrix failure within a

stitched needle); c) transverse specimen at i) 20 N and ii) 2750 N load (dotted boxes show crack closure, and the dotted circle indicates damage within the short cut web matrix).

Figure 8: Visualisation of damage development (11.5 μm voxel), labelled by type and location, as a function of load for a) longitudinal; b) transverse; and c) oblique compression.

Figure 9: Displacement maps (3D visualization) at 750 N, relative to the preloaded tomographs at 20 N for a) Longitudinal; b) Transverse and c) Oblique loading. In each case, the loading axis is parallel to the y-axis. The data have been registered by translation (no rotation) with zero relative displacement at the center of each volume.

Figure 10: Strain maps (displacement field gradients) for a) longitudinal; b) transverse and c) oblique loaded specimens, measured at the largest recorded loads (3500N, 2500N and 1500N for longitudinal, transverse and oblique samples respectively). The principle strains ϵ_{xx} and ϵ_{yy} are shown in (i) and (ii), with (iii) shear strain (ϵ_{xy}) and (iv) maximum principle strain (ϵ_{\max}).

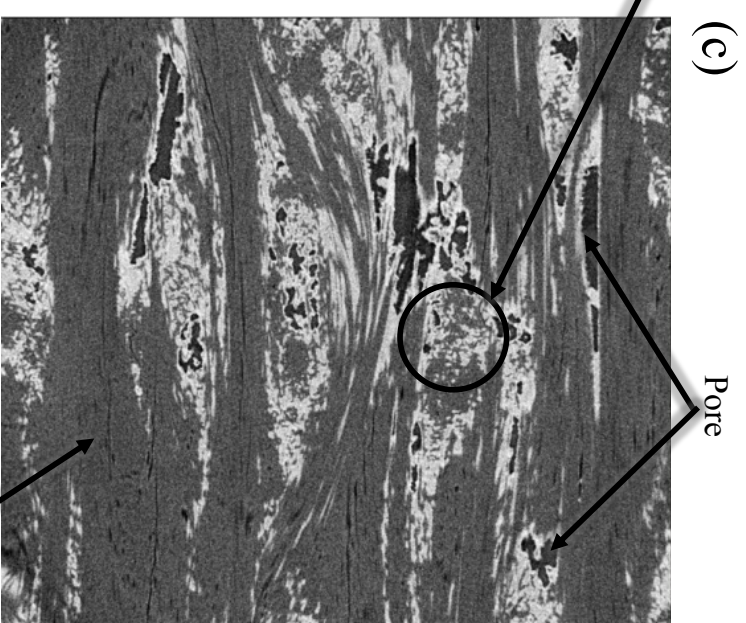
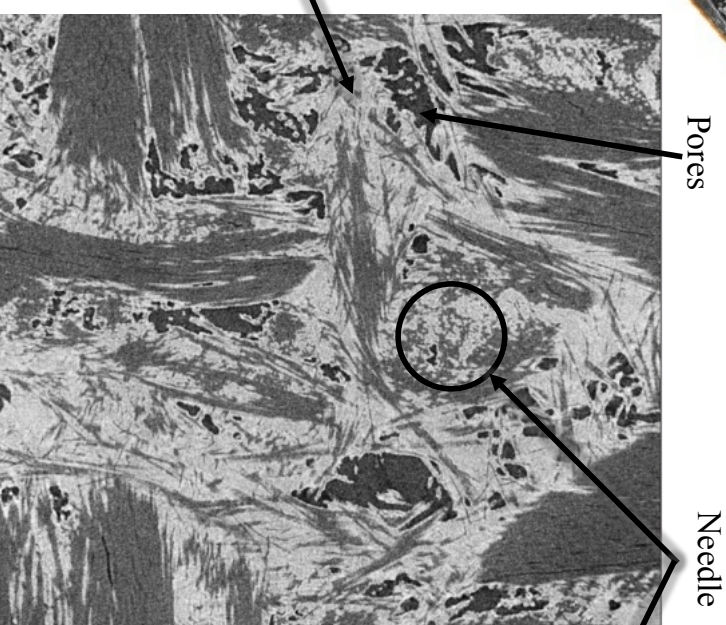
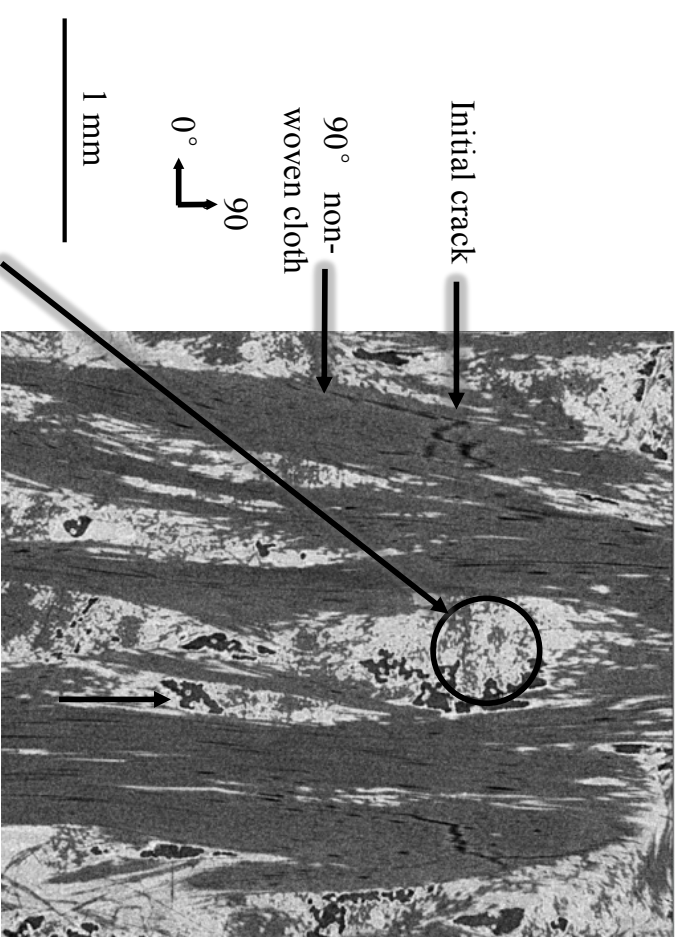
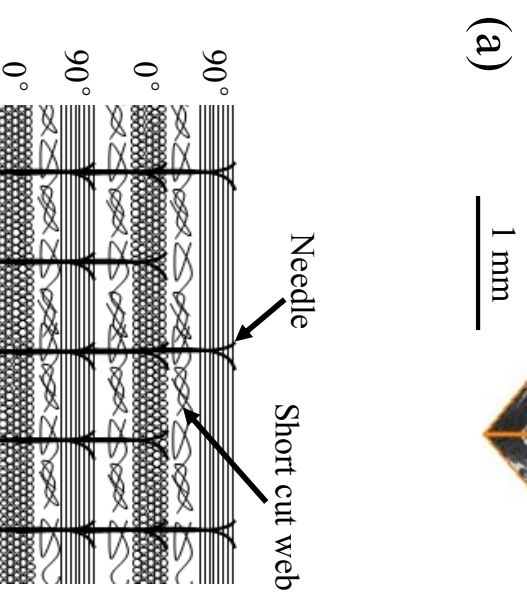
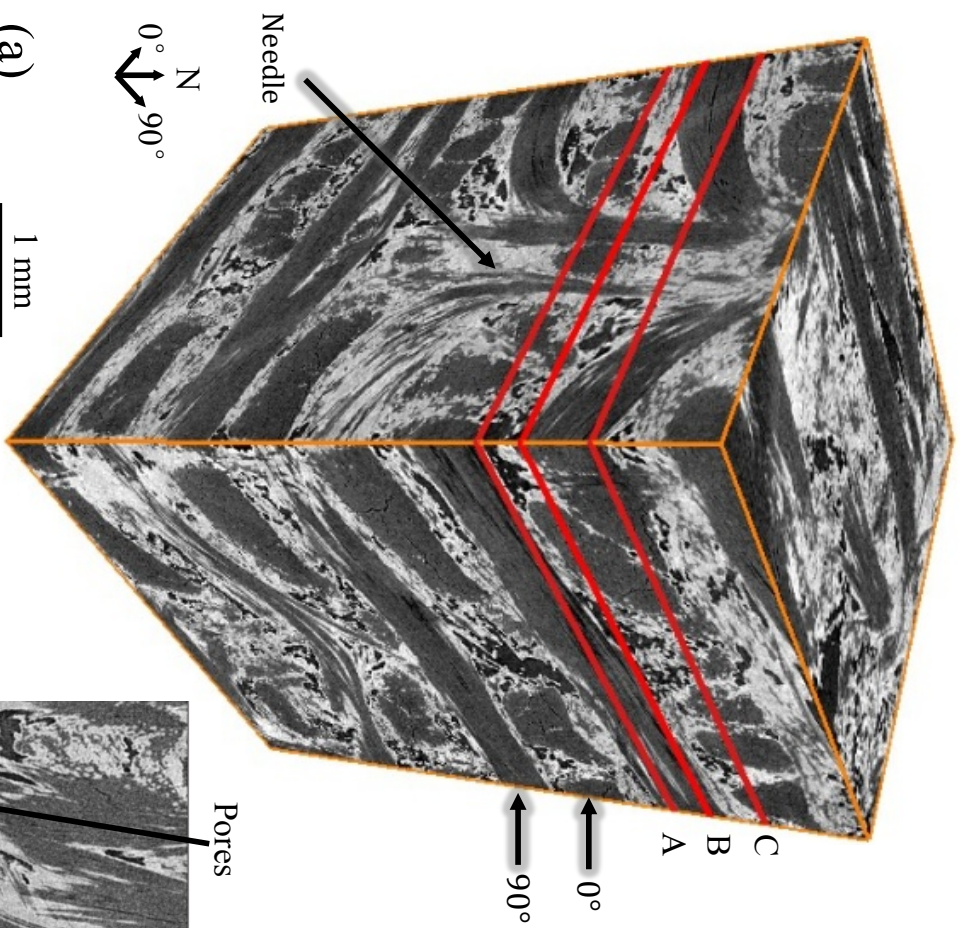
Figure 11: Three dimensional visualization of the effect of needles on the final damage evolved under longitudinal compression: a) maximum principal strain (red) and needles (blue), with slices of the data at the positions of the 90° cloths in (1) to (4); b) observed cracking compared with needles in the same locations.

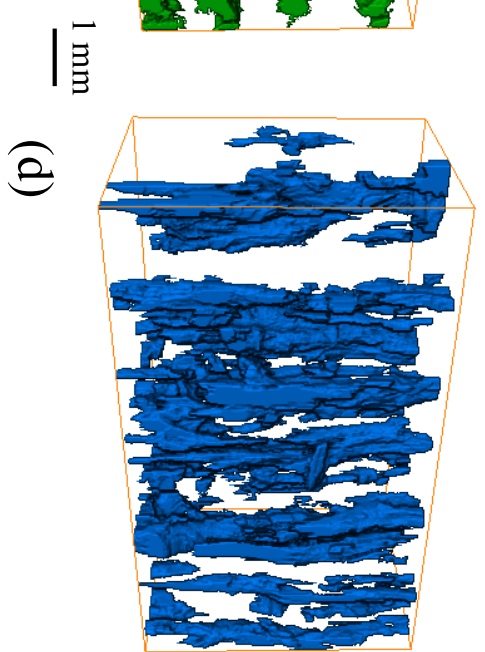
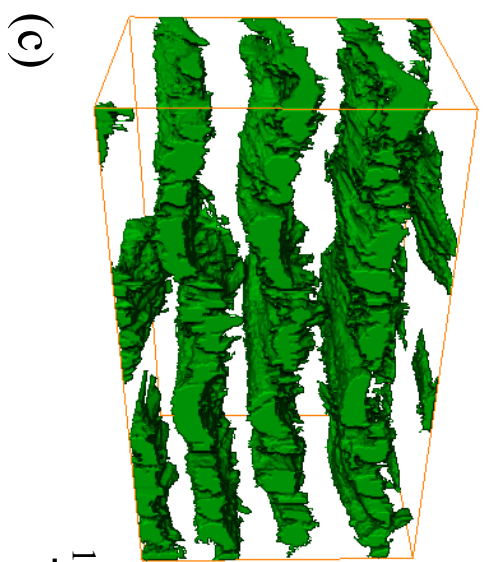
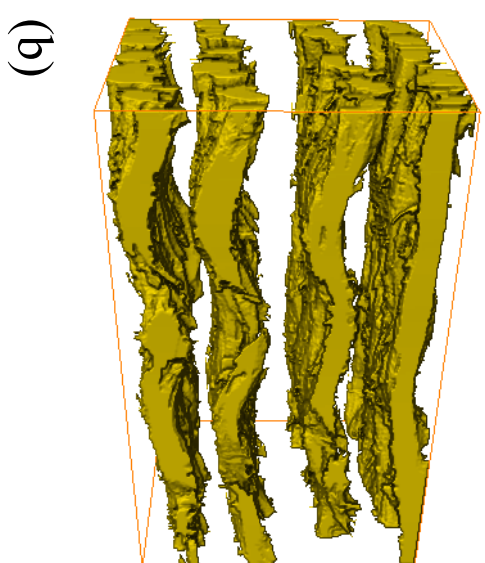
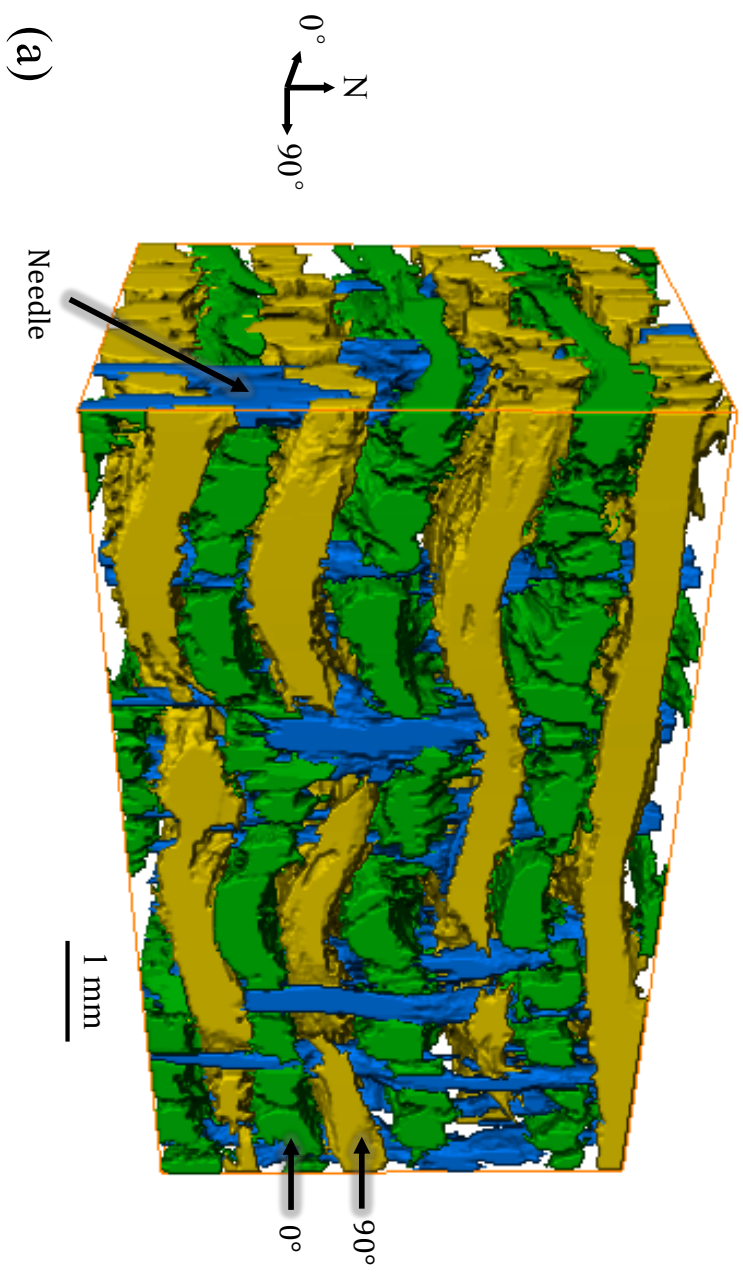
Figure 12: Schematic diagrams for the progressive development of damage under a) longitudinal; b) transverse and c) oblique compressive loading.

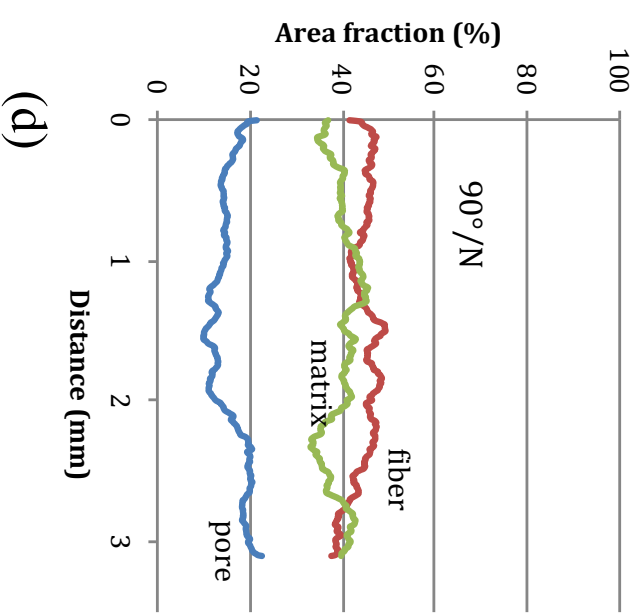
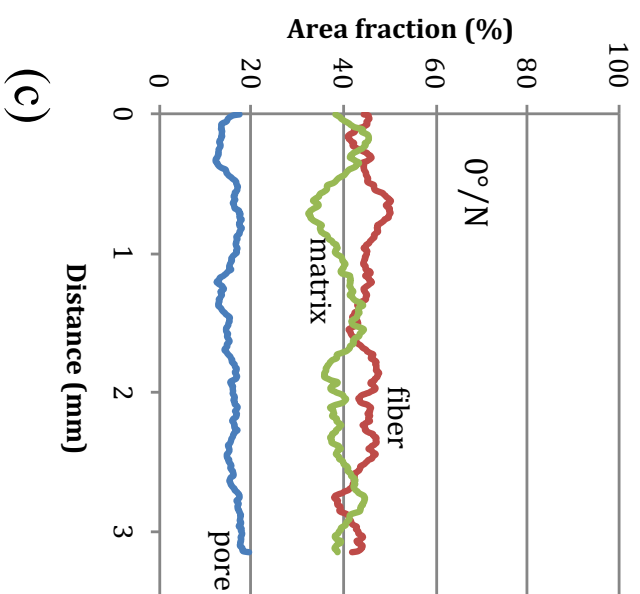
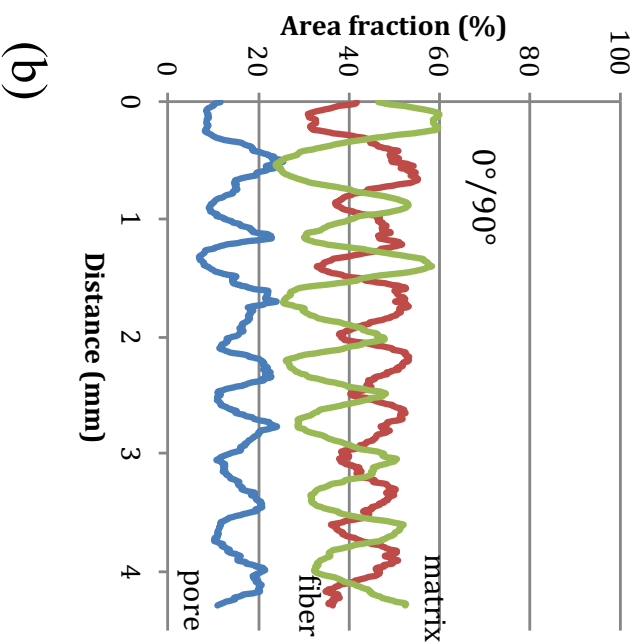
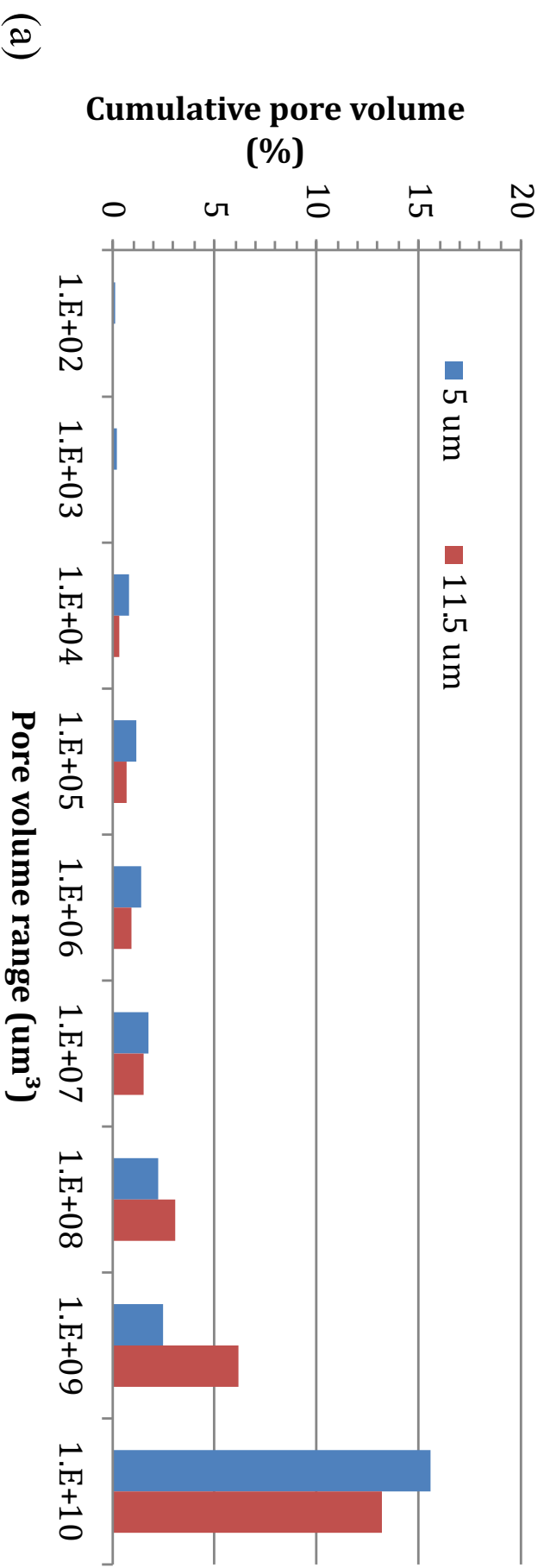
8 Tables

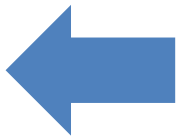
Table 1: Porosity, carbon fiber volume fraction and matrix volume fraction

Method	Porosity (%)	Fiber volume fraction (%)	Matrix volume fraction (%)
Gravimetric analysis [2]	15.73	44.4	39.8
XCT (11.5 μm)	13.13	47.3	39.6
XCT (5 μm voxel)	15.57	44.6	39.8

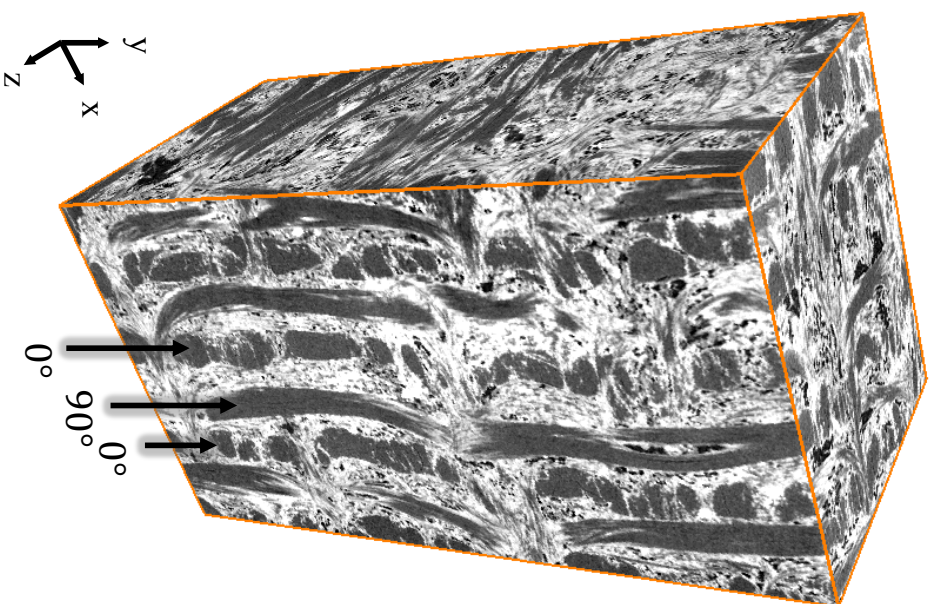
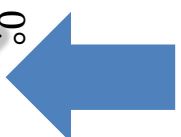
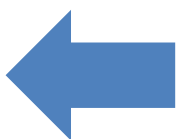




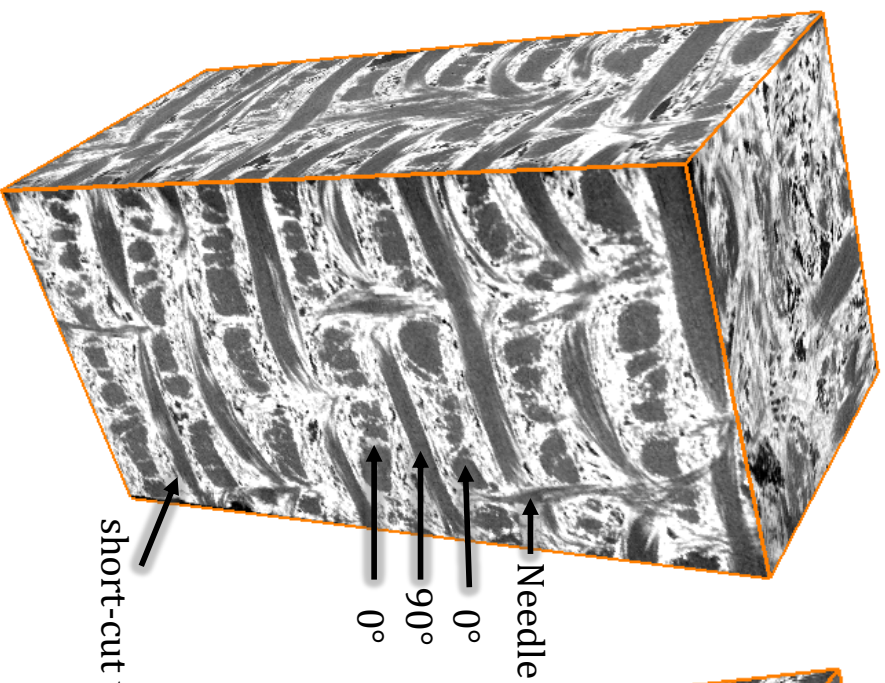




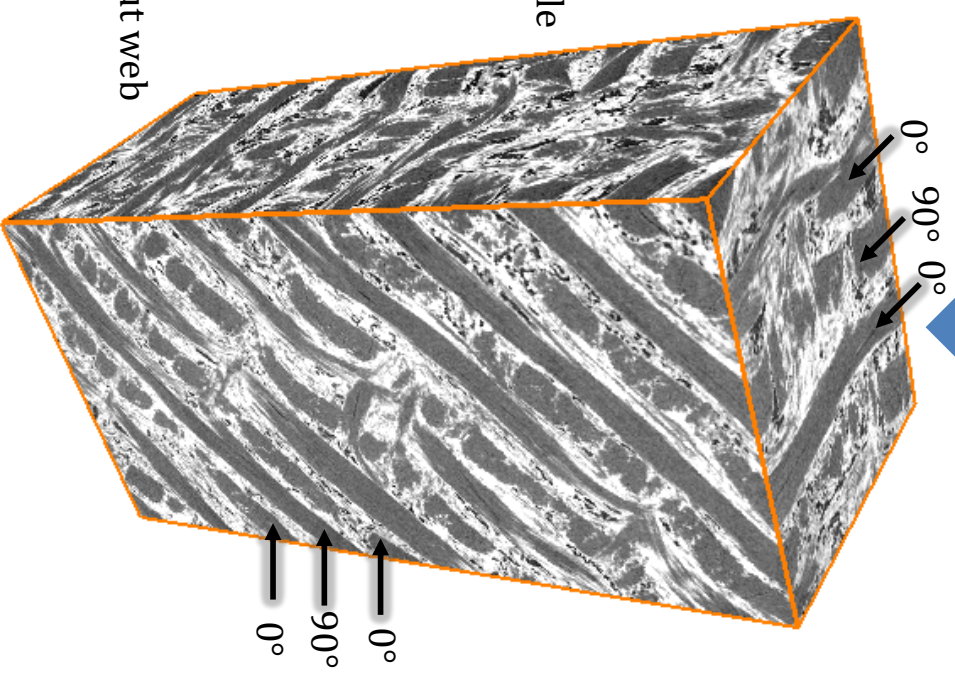
2 mm



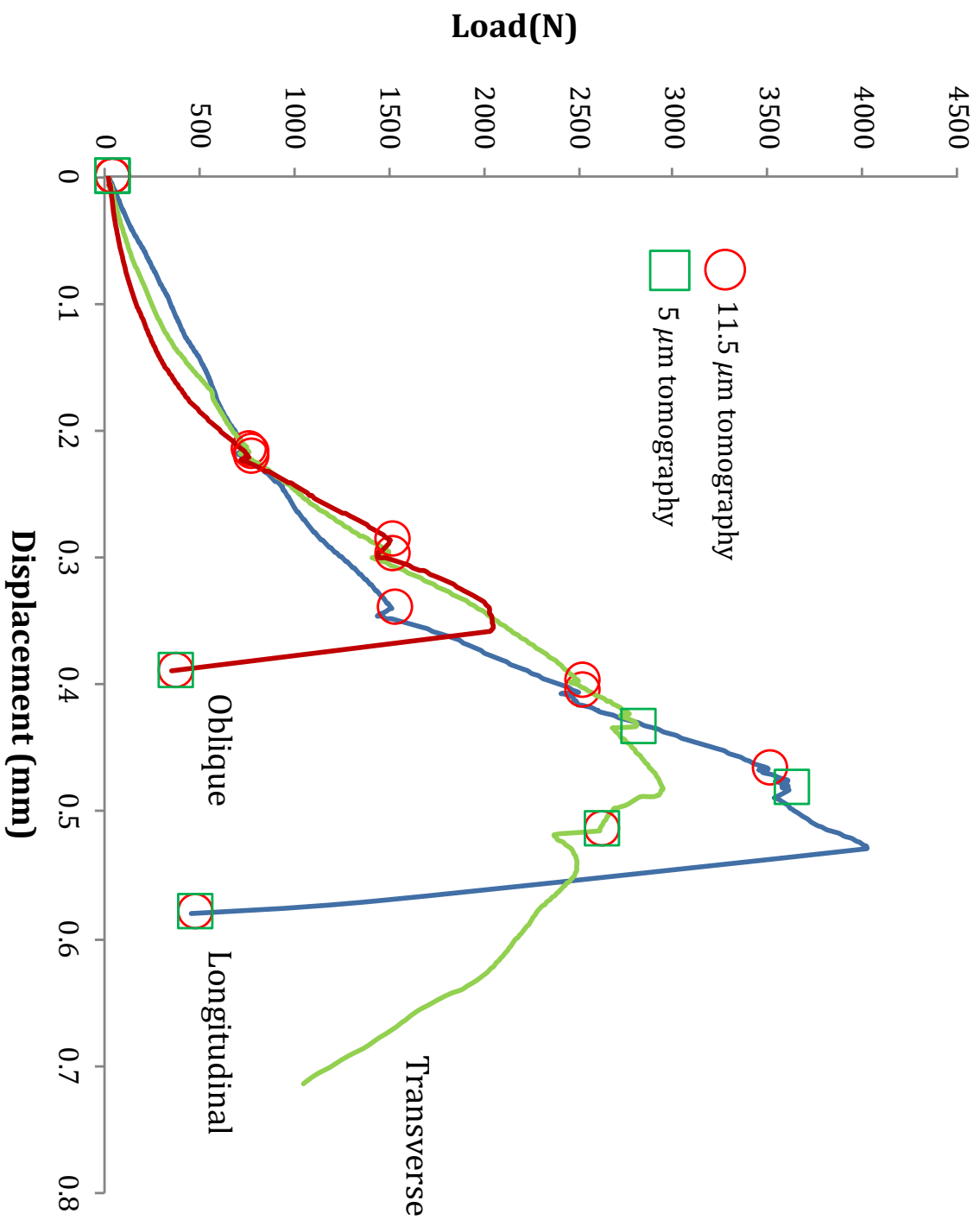
(a) Longitudinal

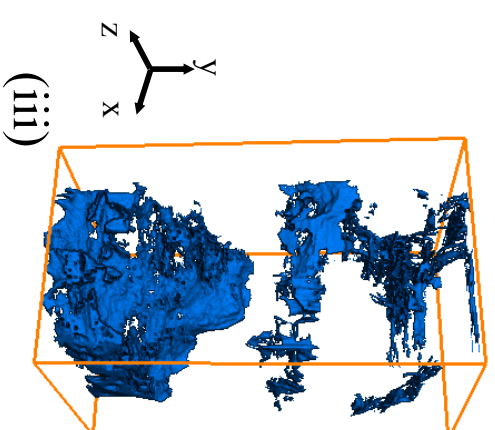
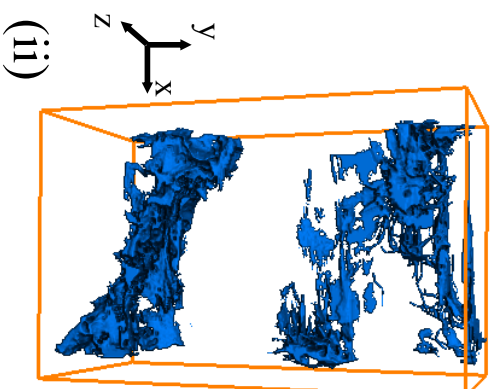
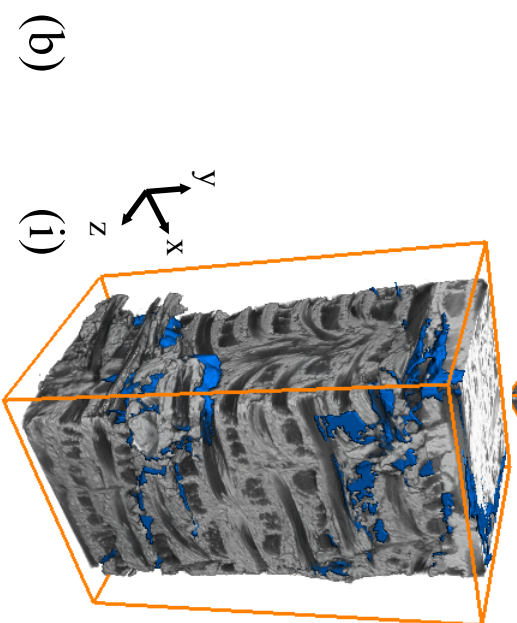
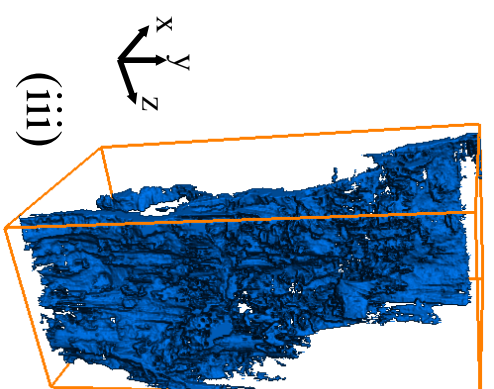
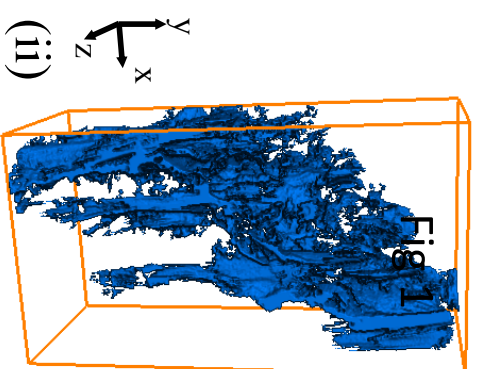
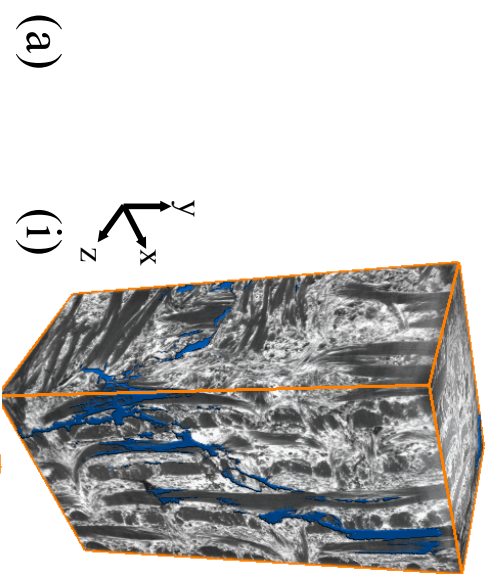


(b) Transverse

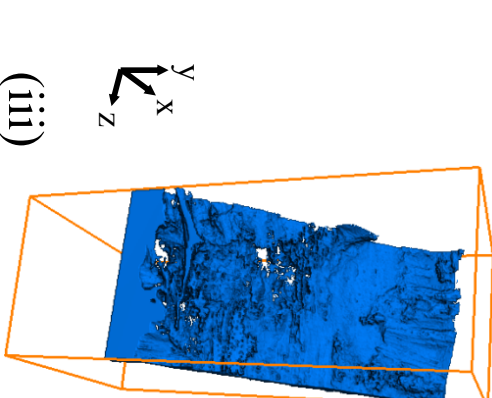
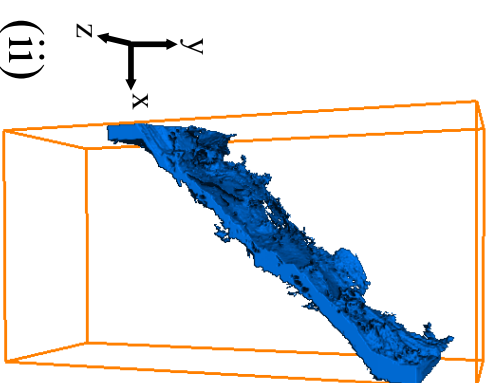
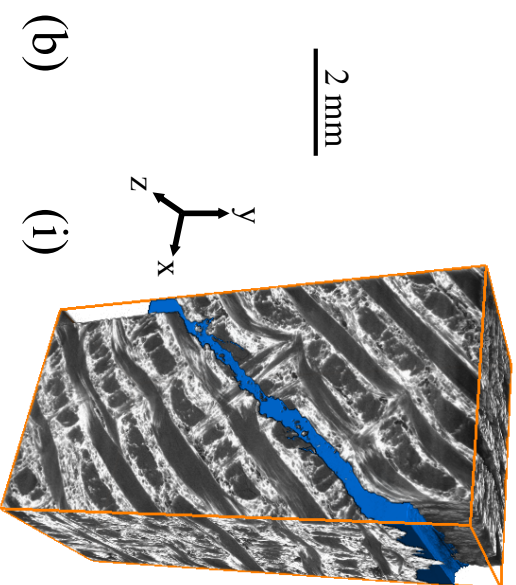


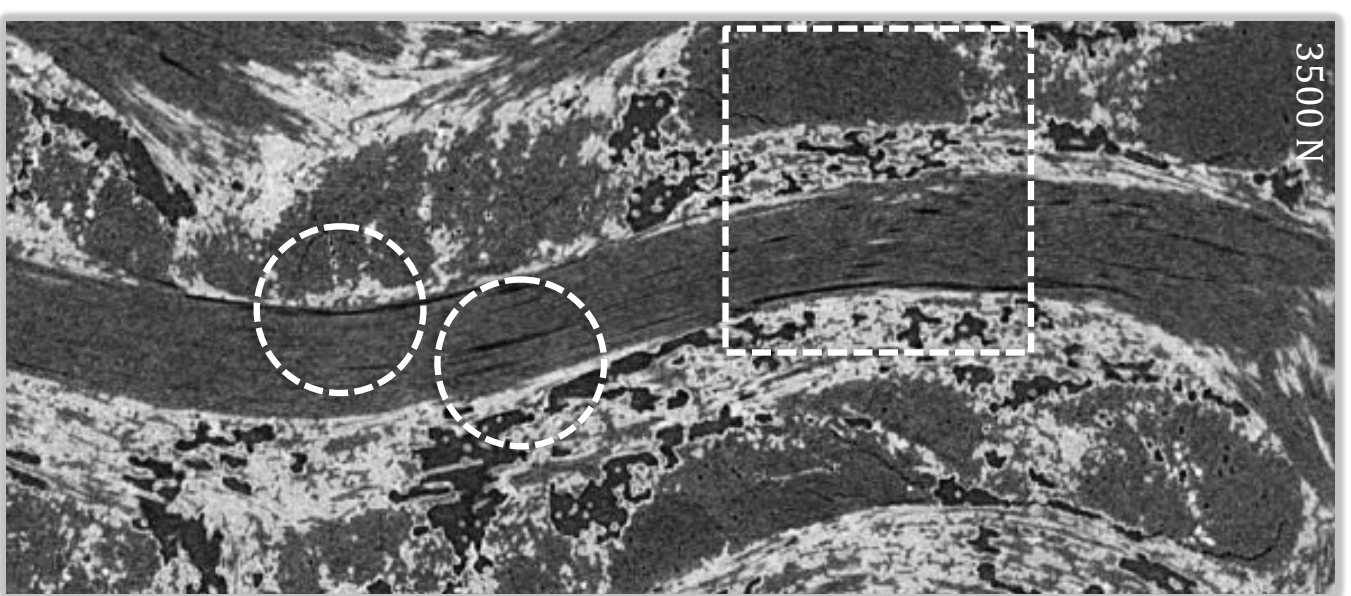
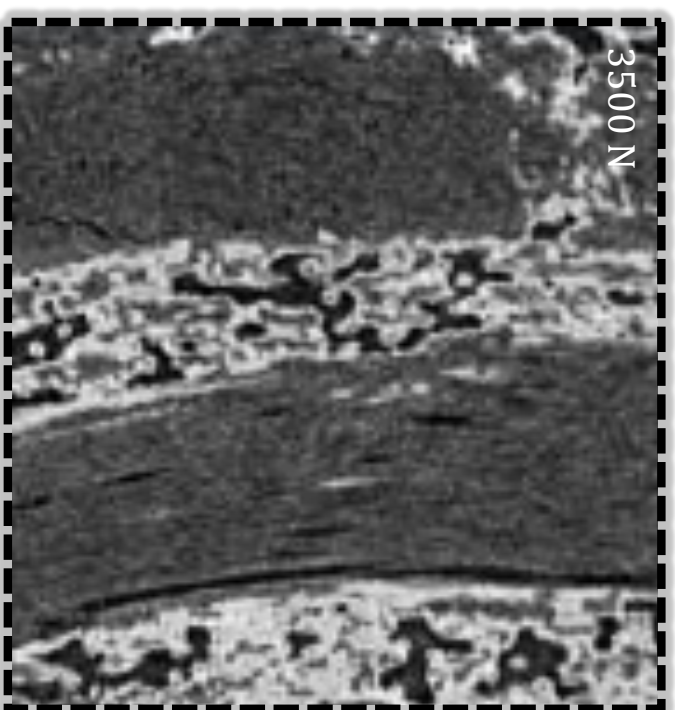
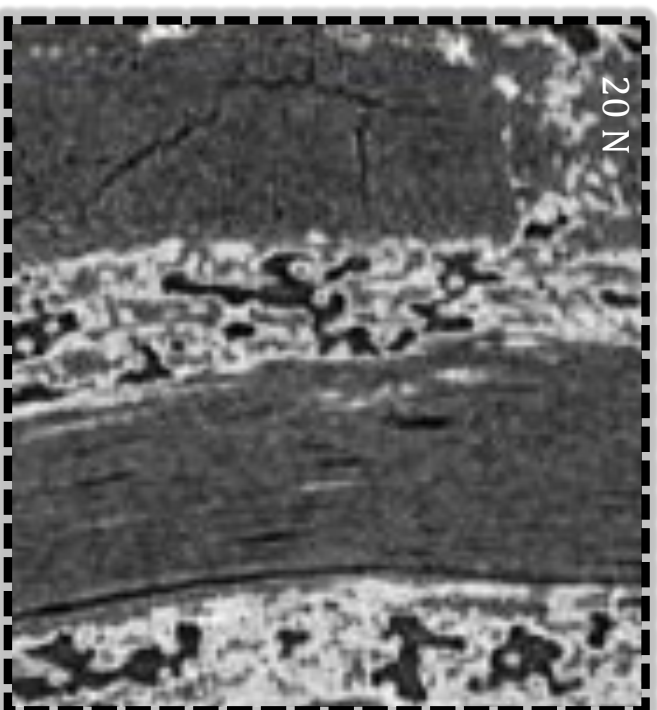
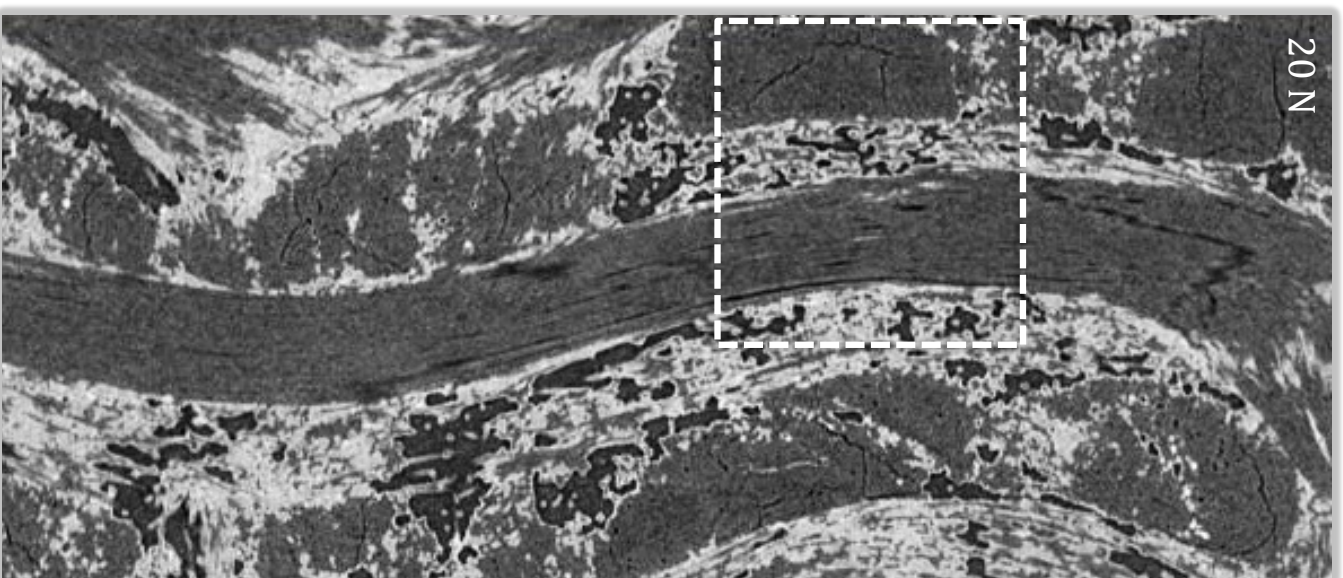
(c) Oblique

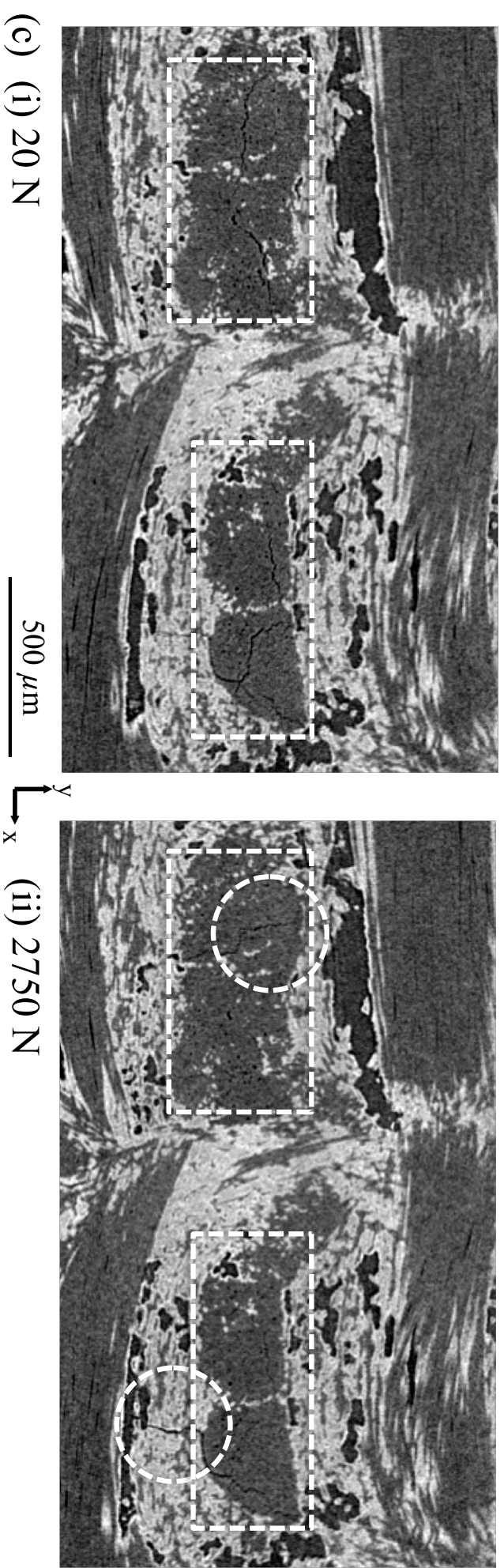
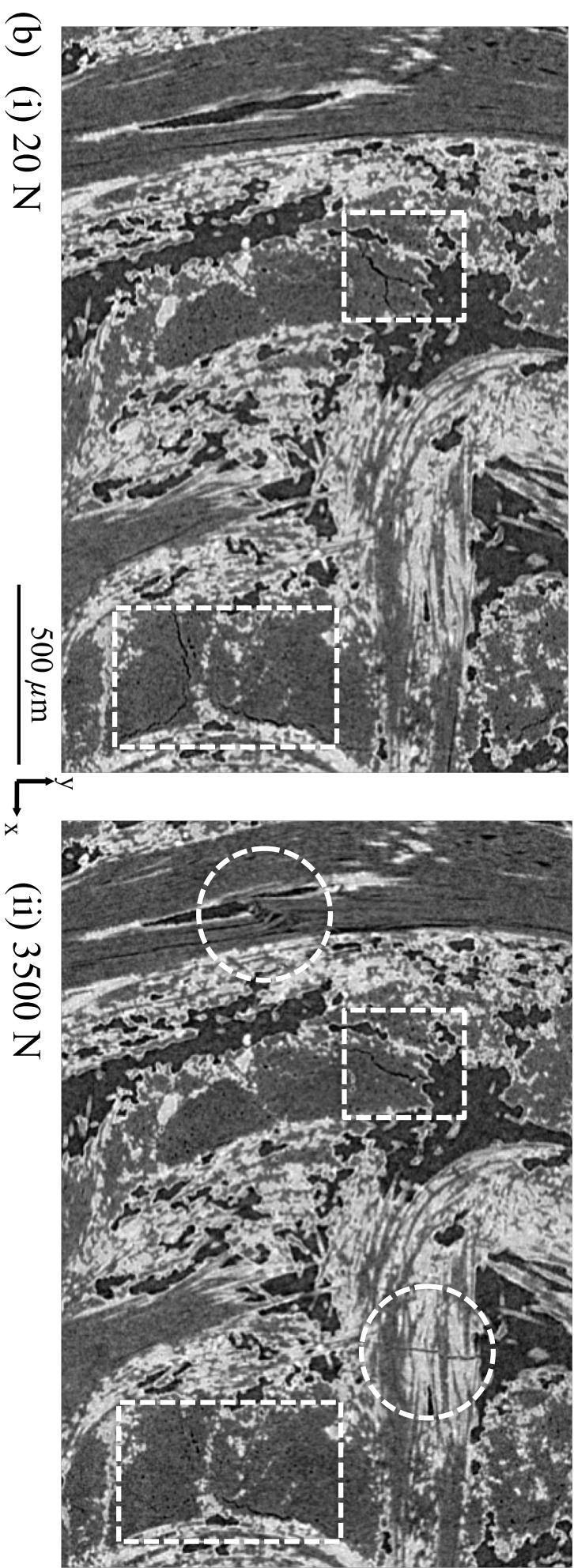


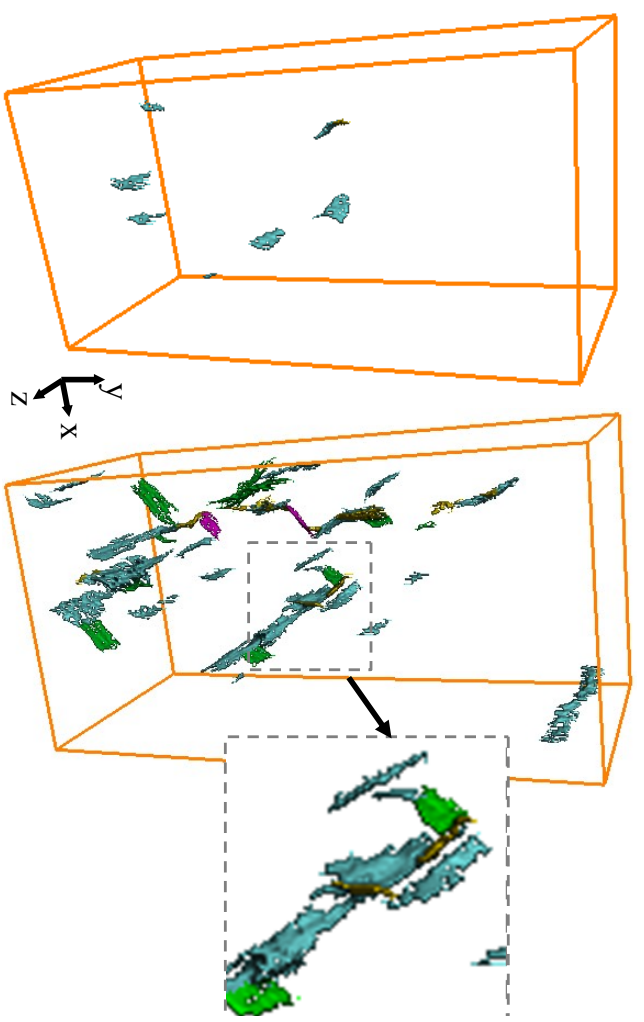
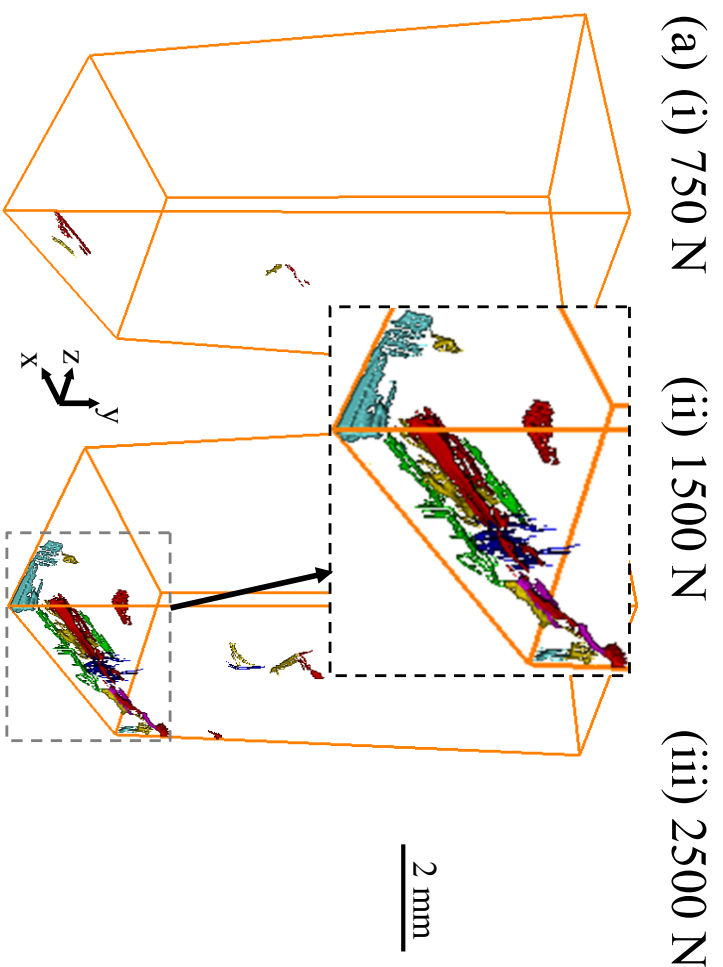
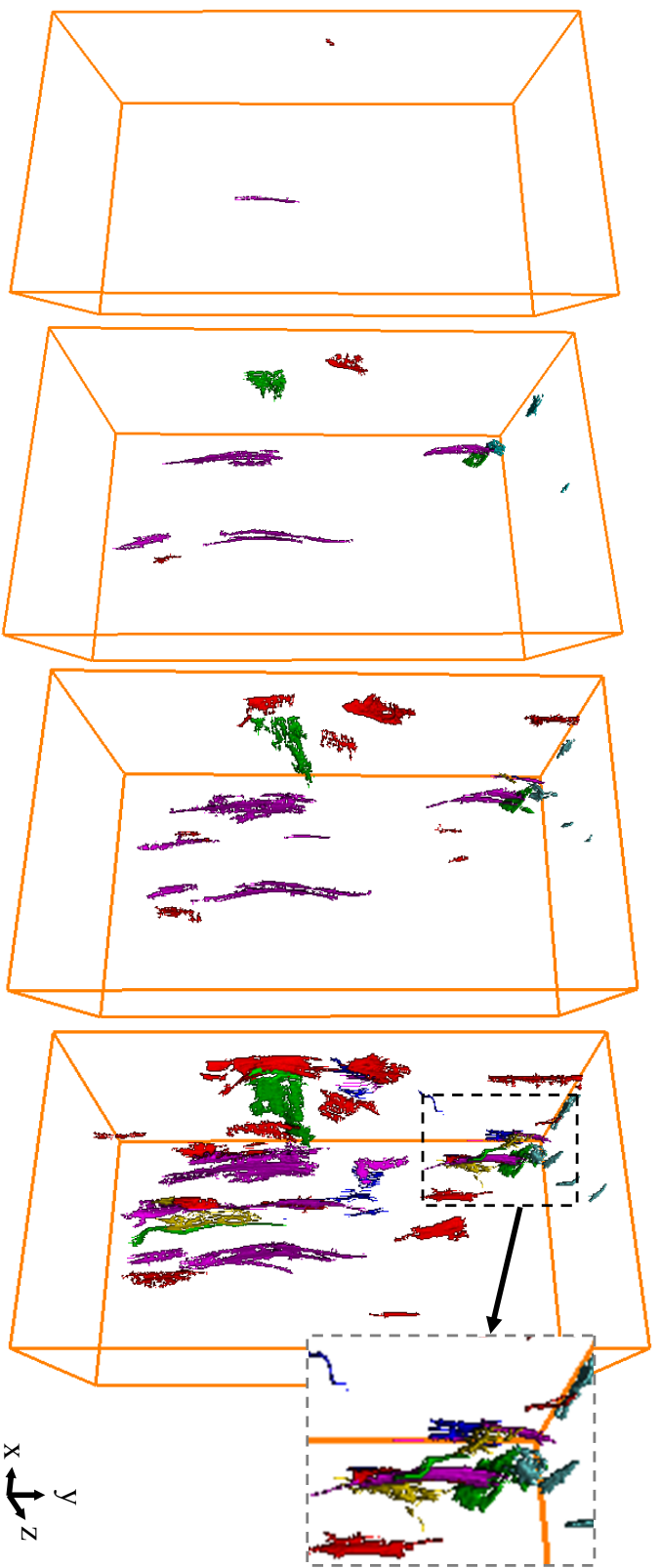
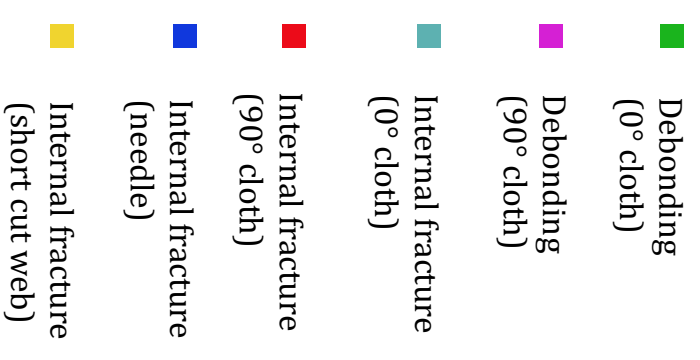


2 mm









(b) (i) 1500 N (ii) 2500 N (c) (i) 750 N (ii) 1500 N

